Applied Physics Letters

RESEARCH ARTICLE | SEPTEMBER 13 2023

Growth of magnetooptical cerium-substituted yttrium iron garnet on yttrium aluminum garnet using ion beam sputtering

Yuki Yoshihara ; Kazushi Ishiyama; Toshiaki Watanabe; Pang Boey Lim ; Mitsuteru Inoue;
Caroline A. Ross ; Taichi Goto ✉

Check for updates

Appl. Phys. Lett. 123, 112404 (2023)
https://doi.org/10.1063/5.0161296

View Online
Export Citation
CrossMark

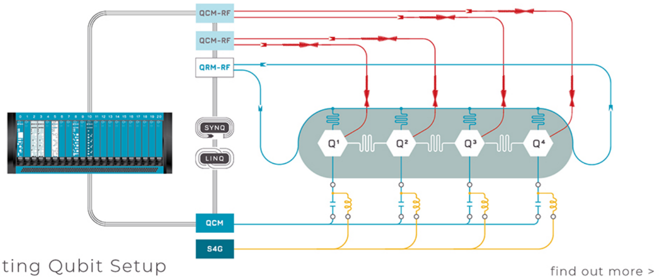

AIP Publishing

Applied Physics Letters ARTICLE pubs.aip.org/aip/apl

Growth of magnetooptical cerium-substituted yttrium iron garnet on yttrium aluminum garnet using ion beam sputtering

Cite as: Appl. Phys. Lett. **123**, 112404 (2023); doi: 10.1063/5.0161296
Submitted: 9 June 2023 · Accepted: 24 August 2023 ·
Published Online: 13 September 2023

Yuki Yoshihara,[1,2,3] Kazushi Ishiyama,[1] Toshiaki Watanabe,[4] Pang Boey Lim,[3] Mitsuteru Inoue,[1]
Caroline A. Ross,[5] and Taichi Goto[1,a)]

AFFILIATIONS

[1] Research Institute of Electrical Communication, Tohoku University, 2-1-1 Katahira, Aoba, Sendai, Miyagi 980-8577, Japan
[2] Graduate School of Engineering, Tohoku University, 6-6 Aramaki, Aoba, Sendai, Miyagi 980-8579, Japan
[3] Toyohashi University of Technology, 1-1 Hibarigaoka, Tempaku, Aichi 441-8580, Japan
[4] Shin-Etsu Chemical Co., Ltd., 2-13-1 Isobe, Annaka, Gunma 379-0195, Japan
[5] Department of Materials Science and Engineering, Massachusetts Institute of Technology, 77 Massachusetts Avenue, Cambridge, Massachusetts 02139, USA

a) Author to whom correspondence should be addressed: taichi.goto.a6@tohoku.ac.jp

ABSTRACT

Cerium-substituted yttrium iron garnet (Ce:YIG, $Ce_{0.9}Y_{2.1}Fe_5O_{12}$) was epitaxially grown on a (111)-oriented yttrium aluminum garnet (YAG) substrate using radio frequency ion beam sputtering. Magnetic hysteresis loops, transmissivity spectra, and magnetooptical (MO) responses, including Faraday rotation and Faraday ellipticity, were measured. The structural properties of the grown Ce:YIG were characterized using the x-ray rocking curve, reciprocal space map, pole figure, and x-ray reflectivity. X-ray photoelectron spectrometry revealed a dominant Ce^{3+} state in the grown Ce:YIG, but the transmission electron microscopy images showed columnar growth of Ce:YIG. This study demonstrates integration of epitaxial Ce:YIG on YAG, marking a significant step toward the fusion of MO garnets and laser crystals.

Magnetooptical (MO) materials have been developed for various applications, such as optical isolators,[1–3] holographic media,[4,5] displays,[6,7] and magnetic-field observation devices.[8,9] In addition, their MO response, including the MO Kerr and Faraday effects, is useful in spintronics and magnonics research to characterize the nanoscale dynamics of spin[10–13] and domain wall states[14,15] in magnetic devices. These applications take advantage of the large MO response and low optical absorption of magnetic garnet films. Using these features, we recently demonstrated an MO Q-switching device using a magnetic garnet film,[14,16,17] showing a high-power pulse in a compact device. Magnetic garnet film fabrication on laser crystals is critical to improving the performance of this device due to its short cavity length, low optical loss, and robustness. Several studies have reported magnetic garnet film growth on yttrium aluminum garnet (YAG) substrates, known as laser crystals, with Nd doping. For instance, Mee *et al.*[18] demonstrated yttrium iron garnet (YIG) growth on a YAG (100) substrate using chemical vapor deposition (CVD). Sposito *et al.*[19] and Krysztofik *et al.*[20] used pulsed laser deposition (PLD) for the growth of YIG/YAG. In addition, Wang *et al.*[21] demonstrated YIG/YAG (111). Despite a ∼3% lattice mismatch, they reported a smooth surface and good crystallinity for the 36-nm thick YIG. Bi and Tb-substituted YIG, and Sm, Ho, Er, and Tm-substituted YIG were grown on a YAG (111) substrate[22,23] to obtain strain-induced perpendicular magnetic anisotropy (PMA). However, the MO response of the iron garnet grown on the YAG (111) substrate was degraded compared to the growth of the same material on a gadolinium gallium garnet (GGG) substrate.[24,25] Furthermore, an attempt to fabricate Ce-substituted YIG (Ce:YIG) on YAG[26] was unsuccessful because of the formation of CeO_2. Hence, in this study, we investigated the MO response of Ce:YIG on YAG by characterizing its crystalline and electronic structures, and its magnetic, optical, and MO properties.

A Ce:YIG film was grown on a (111)-oriented 0.5 × 10 × 10 mm^3 YAG substrate. The substrate was double side polished without an anti-reflection coating. The lattice constant of YAG substrates ($a_{\rm YAG}$) has previously been reported to be 1.2006 nm[27] or 1.201 nm.[28] Ce:YIG was also deposited on a 1-in. diameter 0.725 mm thick Si (100) substrate as a reference. All the substrates were sonicated in isopropanol (IPA), acetone, and de-ionized (DI) water for cleaning.

The samples were deposited using a radio frequency ion beam sputtering (RF-IBS) system (RMTec, RM17-0010) with a base and working pressure of 4×10^{-5} and 3×10^{-2} Pa, respectively. 8 sccm of O_2 was blown onto the samples during deposition. The substrates were heated to 810 ± 30 °C using a lamp heater with a set temperature of 900 °C and rotated at 4.3 rpm to ensure film uniformity. The substrate heating temperature was optimized according to previous reports on growing Ce:YIG by PLD at a temperature range of 615–815 °C.[15,24,29] This temperature range is close to that used in the post-annealing process for preparing polycrystalline Ce:YIG on non-garnet substrates.[30,31] In such cases, the significant difference in thermal expansion coefficient between YIG (1×10^{-5} K^{-1}) and non-garnet substrates, such as fused-silica (6×10^{-5} K^{-1}), generates film cracks and delamination. However, the thermal coefficient of YAG (0.8×10^{-5} K^{-1})[32] is close to that of YIG; hence, we observed no cracks or delamination in our sample. A 4-inch diameter sintered $\rm Ce_{1.0}Y_{2.5}Fe_5O_x$ (Furuuchi Kagaku Co.) target was used. The ion beam voltage and current were 800 V and 36 mA, respectively. 10 and 14 sccm Ar flowed to the ion gun and a low-frequency neutralizer (LFN), respectively. The ion beam accelerator voltage was 160 V, and RF power was 75 W. These ion beam conditions were the same as those used in our previous report.[30] The deposition rate was 1.54 nm/min.

The sample thickness t was measured using a stylus profilometer (KLA Tencor Alpha-Step IQ) with a stylus force of 12 mg. A length of 500 μm was scanned at a speed of 2 μm/s and a sampling rate of 50 Hz. The composition of the film was measured using an energy-dispersive spectrometer (EDS, Oxford Instruments INCA E250 X-Max) mounted on a scanning electron microscope (SEM, HITACHI SU-8000). The accelerating voltage and emission current were 30 kV and 15 μA, respectively. The working distance was set to 15 mm. The region of observation was magnified by 6000 by SEM for plane scan analysis. The crystalline structure was characterized using an x-ray diffractometer (XRD Rigaku Smartlab). A Cu $K_{\alpha 1}$ (wavelength $\lambda = 0.15418$ nm) radiation source was used with x-ray power of 2 kW. The optical receiving system consisted of a 5.0° Soller slit and high-resolution parallel beam Ge (220) × 2 analyzer. Optical transmissivity was measured using a spectrophotometer (Shimadzu UV-3150) with a double monochromator and randomly polarized lamp source. The scanning speed was set to "slow" mode, with a wavelength resolution of 5 nm. The irradiated spot diameter perpendicular to the sample surface was 2.2 mm. The Faraday rotation (FR) and Faraday ellipticity (FE) spectra and loops were measured using an MO measurement system (JASCO, J-1700FK). This system is based on a rotating polarizer and polarization modulation methods. Sample temperature was maintained at 40 ± 0.5 °C using a Peltier temperature controller to reduce the effects of the temperature dependence of Ce:YIG magnetization. The spot dimension of the irradiated light on the sample was 1×5 mm^2, and a magnetic field of ±5 kOe was applied for each spectrum and loop measurement. Magnetic hysteresis loops were measured using a vibrating-sample magnetometer (VSM, Tamakawa Corp., TM-VSM2050-HGC-TOH), and an ionizing fan (AS ONE Corp., SIB-1DC) was used to suppress the electrostatic noise of the VSM. The electronic binding state of the film was measured using x-ray photoelectron spectroscopy (XPS, Shimadzu Kratos Axis Ultra). The x-ray source was monochromated Al K_α with an energy of 1486.69 eV, and the x-ray output voltage, current, and power were 15 kV, 10 mA, and 150 W, respectively. The surfaces of the measured samples was etched for 5s with 2 kV Ar sputtering to avoid the influence of surface contamination and oxidation. The charge correction shift of the post-etching spectra was acquired using Y 3d doublet peaks corrected by the C 1s peak before etching. Transmission electron microscopy (TEM, JEOL JEM-ARM200F) and element mapping of the cross-sectional images were performed.

The thickness t of Ce:YIG/YAG was 129 ± 4.5 nm. The error indicates the standard deviation of nine repeated measurements. The film composition of $\rm Ce_{0.9\pm0.1}Y_{2.1\pm0.1}Fe_5O_{12-\delta}$ was obtained from EDS measurement. (δ represents oxygen deficiency, which was not measured.) The Y K_α peak was used for EDS composition quantification instead of Y L_α, which overlapped with the Si K_α peak.

The x-ray diffraction scan of Ce:YIG/YAG near the (444) peak is shown in Fig. 1(a). Both substrate and film exhibit a (111) orientation. The Ce: YIG (444) peak is broad and lacks Laue fringes suggesting structural disorder or interface roughness. The peak position of the Ce:YIG film was $2\theta = 50.83°$. Figure 1(b) shows x-ray reflectivity with interference fringes. The curve fitting-derived thickness of Ce:YIG was 120.4 ± 0.1 nm, which is close to the value measured by the profilometer. The estimated density of the Ce:YIG film and YAG substrate was 5.19 ± 0.05 and 4.55 g/cm^3, respectively. The surface roughness of Ce:YIG was 1.52 ± 0.15 nm.

Figure 1(c) shows the pole figure of the (444) peak. Epitaxial growth of Ce:YIG/YAG was observed with four (444) peaks at $\alpha_{\rm ps} = 0°$ and 70.5°. The 12 additional (640) peaks ($\alpha_{\rm ps} = 36.8°$ and 80.8°) generated due to garnet structure deformation[22] are also illustrated. The origin of these (640) peaks is still under discussion. However, it is possible that they could have occurred due to the columnar growth of Ce:YIG, as revealed by the TEM observations discussed below. A pole figure of the YAG substrate is provided in the supplementary material.

A reciprocal space map (RSM) was measured around the 336 peak, as shown in Fig. 1(d). The Ce:YIG is strain-relaxed with respect to the substrate. The in-plane (IP) and out-of-plane (OP) lattice spacing of the Ce:YIG film exceeds that of the YAG, consistent with the expected lattice mismatch of ∼3% between the YAG ($a_{\rm YAG} = 1.201$ nm[28]) and Ce:YIG ($a_{\rm Ce:YIG} = 1.257$ nm,[15] 1.258 nm,[33] and 1.250 nm.[34]) We assume that the Ce:YIG film was rhombohedrally distorted and estimate the strain state of the film from the measured IP and OP lattice spacings. For the rhombohedral unit cell, the lattice parameter $a = b = c = A$, and the lattice corner angle is $\alpha_{cs} = \beta_{cs} = \gamma_{cs} = \theta_{cs}$. The lattice spacing for the (444) and $(\bar{1}\bar{1}2)$ reflections can be calculated using previously reported methods,[35,36] as follows:

$$\frac{1}{d^2{}_{444}} = 48\,\frac{\sin^2\theta_{CS} + 2(\cos^2\theta_{CS} - \cos\theta_{CS})}{A^2(1 - 3\cos^2\theta_{CS} + 2\cos^3\theta_{CS})}, \qquad (1)$$

$$\frac{1}{d^2{}_{\bar{1}\bar{1}2}} = 6\,\frac{\sin^2\theta_{CS} - (\cos^2\theta_{CS} - \cos\theta_{CS})}{A^2(1 - 3\cos^2\theta_{CS} + 2\cos^3\theta_{CS})}. \qquad (2)$$

From the relation $q_x = d^{-1}_{\bar{1}\bar{1}2}$ and $q_z = d^{-1}_{444}$, A and θ_{cs} were calculated. The values of $A = 1.2434$ nm and $\theta_{cs} = 89.838°$ were obtained for

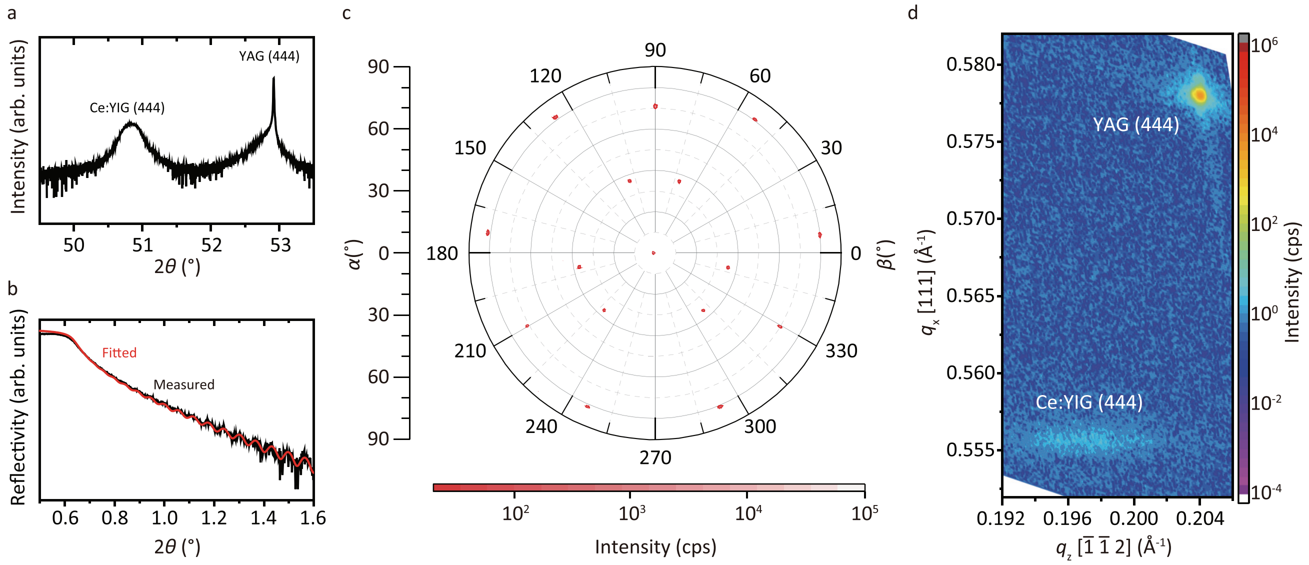

FIG. 1. (a) XRD at around (444) peaks, (b) XRR of Ce:YIG/YAG, and (c) pole figure at (444) peak ($2\theta = 52.955°$). There are no other peaks except the (444) and (888) of the film and substrate. (d) RSM around the (336) substrate peak.

Ce:YIG/YAG, close to the prior reports.[15,33,34] Hence, the film is under an IP compressive strain and tensile OP strain.

The MO properties were obtained from the FR and FE spectra and loops [Figs. 2(a) and 2(b)], after subtracting the FR and FE values of YAG. Figure 2(b) shows the FR and FE loops measured at a wavelength of $\lambda = 1064$ nm after subtracting the paramagnetic background. FR at $\lambda = 1064$ nm was $-0.65°/\mu$m, 50% of the value reported for Ce:YIG/GGG ($-1.3°/\mu$m)[24] and 60% of the value for polycrystalline Ce:YIG/silica ($-1.07°/\mu$m).[30] The transmittivity of Ce:YIG/YAG and YAG is shown in Fig. 2(c). Around a wavelength of $\lambda = 800$ nm, both the FR and FE spectra exhibit a positive and negative peak, respectively. The magnetooptical peak in this region is likely attributable to the charge transition between in Ce^{3+} and Fe^{3+} ions.[24,37] This transition can also be observed as an absorption in the transmittivity spectrum in the same region. Averaged FR and FE spectra and loops are presented in the supplementary material. The inset shows the refractive index n and extinction coefficient κ of Ce:YIG obtained by the spectral fitting simulation software (W. Theiss Hard- and Software, SCOUT version 3.04)[31] based on the Fresnel equation. The n and κ values of the YAG substrate are presented in the supplementary material. The MO figure of merit (FOM), defined as FR divided by the optical absorption, α_{opt}, was obtained. The absorption was

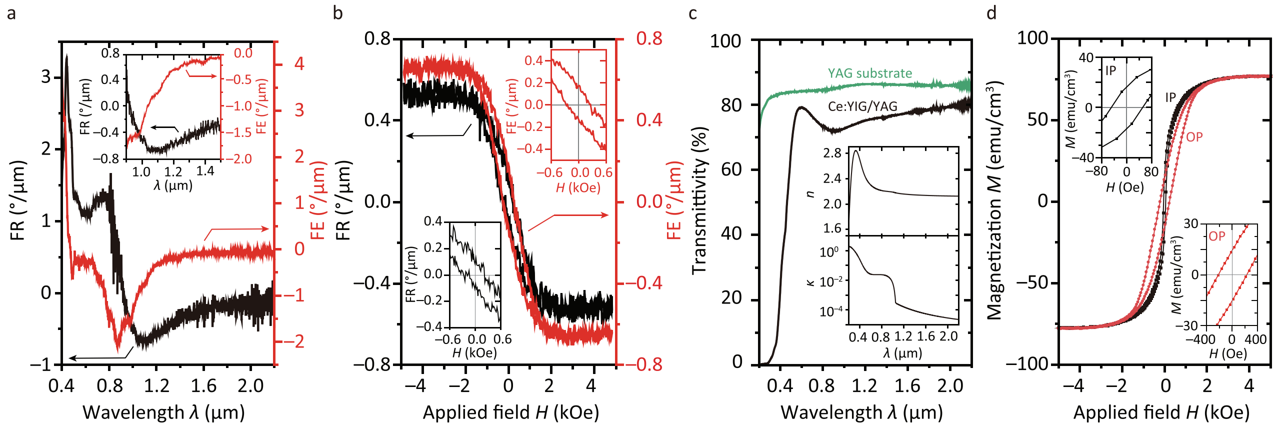

FIG. 2. (a) FR and FE spectra of the Ce:YIG. The FR and FE of the YAG substrate were subtracted. Inset shows the enlarged spectra around the NIR region. (b) FR and FE loops of the Ce:YIG at $\lambda = 1064$ nm. Insets show the enlarged loops around near-zero fields. (c) Transmittivity spectra of the Ce:YIG/YAG and YAG substrate. Insets show the refractive index n and extinction coefficient κ of the Ce:YIG film. (d) IP and OP magnetic hysteresis loops of the Ce:YIG/YAG. Insets show M_r and H_c. The paramagnetic component was subtracted.

expressed as α_{opt} (dB/cm) = 10×log$_{10}$[exp (4$\pi\kappa$×0.01/λ)]. The MO FOM was 49.7°/dB at $\lambda = 1064$ nm, 68% of that of polycrystalline Ce:YIG/silica.[30] The MO FOM at $\lambda = 1550$ nm was 126.5°/dB. This value is 13%–37% of that of Ce:YIG/GGG single crystalline films.[24,34]

The magnetic hysteresis loops measured by VSM are shown in Fig. 2(d). The saturation magnetization M_s was 77.4 emu/cm^3, 56%–77% of that of Ce:YIG/GGG (100–138 emu/cm^3).[25,38] The reduced M_s may be a result of the presence of tetravalent Ce (described below) and its associated oxygen deficiency or divalent Fe, or due to structural imperfections. The coercivities were $H_{c,IP} = 50$ Oe and $H_{c,OP} = 222$ Oe for IP and OP, respectively. The area difference between the hysteretic IP and OP VSM loops showed a total anisotropy energy U^{VSM} of 2.39 × 10^4 erg/cm^3 corresponding to an magnetic anisotropy field of $H_A^{VSM} = 618$ Oe.

The magnetic anisotropy energy U^{cal} in Ce:YIG/YAG is the total of shape anisotropy K_{shape}, magnetocrystalline anisotropy K_{cry}, and magnetoelastic anisotropy K_{ela}. The magnetic anisotropy energy U^{cal}, which is the energy difference between the IP and OP magnetization directions, and the magnetic anisotropy field H_A^{cal} were derived using the following equations:[35]

$$U^{cal} = K_{cry} + K_{ela} + K_{shape} = -\frac{K_1}{12} + \frac{9}{4}\lambda_{111}c_{44}\left(\frac{\pi}{2} - \theta_{CS}\right) - 2\pi M_s^2, \tag{3}$$

$$H_A^{cal} = \frac{2U}{M_s}. \tag{4}$$

The magnetostriction constant $\lambda_{111} = 12.9 \times 10^{-6}$ for the Ce:YIG ($Ce_{0.9}Y_{2.1}Fe_5O_{12}$) was obtained by interpolation using the predicted value $\lambda_{111,CeIG} = 50 \times 10^{-6}$ (Ref. 39) for $Ce_3Fe_5O_{12}$ and the experimental value $\lambda_{111,YIG} = -3 \times 10^{-6}$ (Ref. 40) for $Y_3Fe_5O_{12}$. K_1 and c_{44} are the first-order cubic magnetocrystalline anisotropy and shear modulus, respectively. Literature values for bulk YIG were used for these two constants ($K_1 = -610$ J/m^3 = -6100 erg/cm^3; $c_{44} = 76.6$ GPa = 7.66 × 10^{11} dyn/cm^2).[35,41] M_S and θ_{cs} were obtained from the VSM and XRD results shown above ($M_s = 77.4$ emu/cm^3 and $\theta_{cs} = 89.838°$ [= 1.5679 rad], respectively). These values yield an anisotropy energy U^{cal} of Ce:YIG of 2.73 × 10^4 erg/cm^3 and $H_A^{cal} = 705$ Oe. The magnetoelastic anisotropy K_{ela} is the largest contribution to U^{cal} (6.44 × 10^4 erg/cm^3), and the shape anisotropy K_{shape} is −3.75 × 10^4 erg/cm^3, with the magnetocrystalline anisotropy K_{cry} of 5 × 10^2 erg/cm^3. The calculated U^{cal} is within 12% of U^{VSM} obtained from the hysteresis loops. This is a reasonable agreement considering the multiple approximations, particularly in the interpolation of λ_{111}, which is based on a value for $\lambda_{111,CeIG}$ that is itself extrapolated from a measurement of Ce:YIG with only a 1% Ce substitution.[39] The agreement suggests that growth-induced anisotropy[15,42–45] resulting from site ordering of the cations during film growth plays a minor role.

The electronic states were measured using XPS, as shown in Fig. 3. In the Ce 3d peak [Fig. 3(b)], the Ce^{3+} components were dominant. The origin of the MO enhancement of Ce:YIG arises from the charge transition of Ce^{3+}–Fe^{3+}, and the presence of Ce^{4+} increases absorption and forms cerium oxide (ceria) in the film without contributing to the MO properties.[30,46] The Ce 3d$_{3/2}$ peak at 918 eV is known as the "fingerprint" peak of Ce^{4+}. The ratio of Ce^{3+} and Ce^{4+} for the Ce:YIG film was calculated from the fitted peak regions using software CasaXPS,[47] yielding Ce^{3+}:Ce^{4+} = 87:13. The Fe LMM and Ce MNN regions in Ce 3d and Fe 2p are Auger electron peaks. Other spectra showing Fe 2p, Y 3d, and O 1s were similar to that of the reported Ce:YIG (Ref. 30).

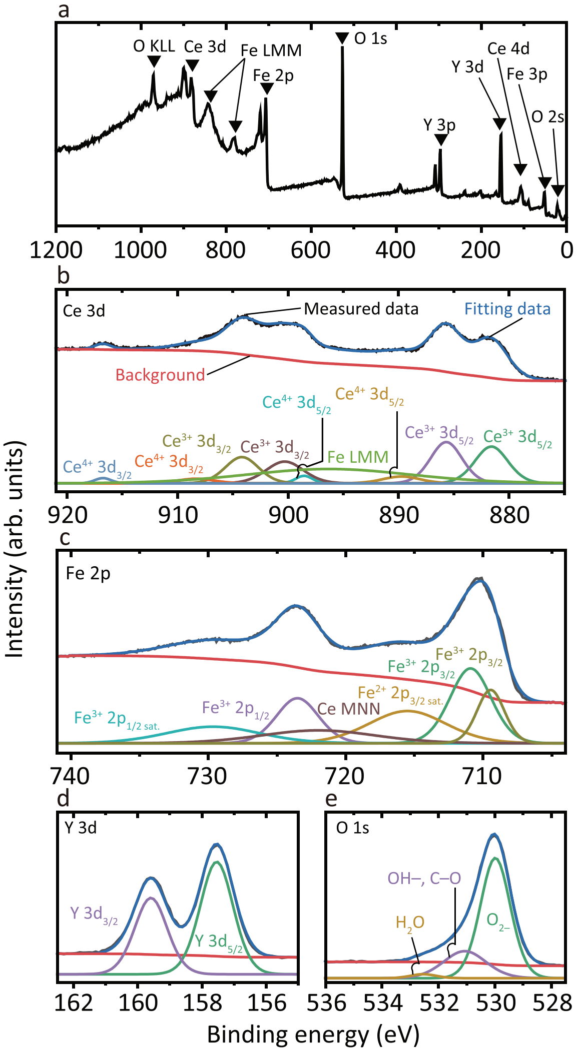

FIG. 3. XPS spectra of the Ce:YIG film. (a) Survey, (b) Ce 3d, (c) Fe 2p, (d) Y 3d, and (f) O 1s spectra of the Ce:YIG/YAG.

Figure 4 shows the cross-sectional high-angle annular dark-field (HAADF) TEM images of Ce:YIG/YAG along a [11$\bar{2}$] zone axis, indicating dislocations and tilting of the Ce:YIG lattice. The inset shows selected area electron diffraction (SAD) images of the Ce:YIG film region. The low-magnification image [Fig. 4(b)] shows columnar growth. The defects and resulting columnar growth are attributed to lattice mismatch between the Ce:YIG and the YAG.

Elemental mapping, as shown in Figs. 4(c)–4(h), shows the Ce, Y, Fe, O, and Al distributions in the film and substrate. A uniform distribution of O was observed, but Ce is enriched within small 3–5 nm diameter particles near the film-substrate interface, corresponding to a deficiency in Fe. These may form to relax lattice mismatch strain at the interface or due to excess Ce. The Ce-rich oxide, likely ceria,

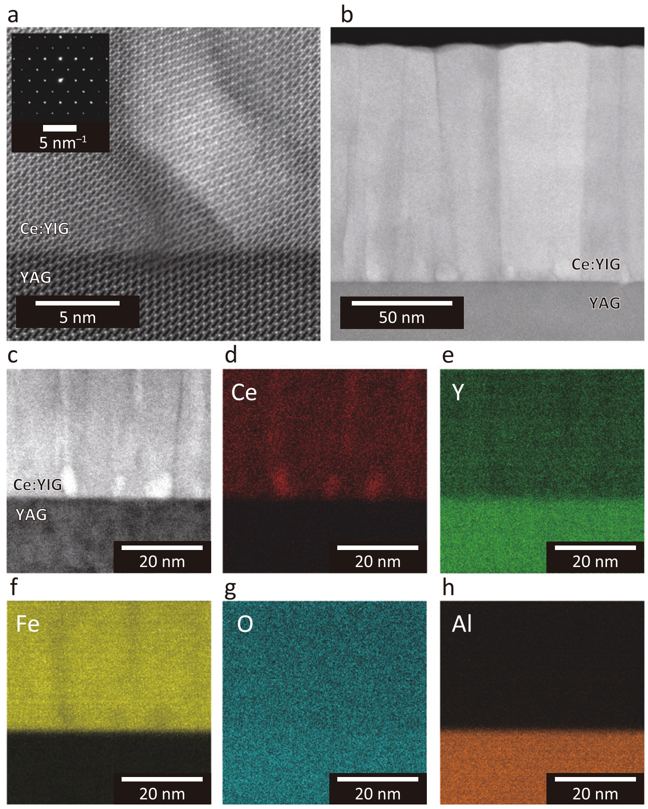

FIG. 4. (a) Cross-sectional HAADF TEM images of the Ce:YIG/YAG, along [11$\bar{2}$] zone axis. Inset shows the SAD image. (b) Wide view image. (c) Scanning TEM image, and TEM EDS element mapping of (d) Ce, (e) Y, (f) Fe, (g) O, and (h) Al.

is expected to reduce the FR and M_s compared to non-defective Ce:YIG/GGG.[24,25] These particles may also act as pinning sites for magnetic domain walls, raising the coercivity H_c.

In conclusion, a Ce:YIG film of $t = 129$ nm was epitaxially grown on a YAG (111) substrate using RF-IBS. The Ce:YIG film grew as a crystalline epitaxial film with lattice defects. Small 3–5 nm Ce-rich nanoparticles, likely ceria, form at the film–substrate interface. These particles may form in order to relax the lattice mismatch strain and are expected to reduce the FR and M_S compared with Ce:YIG grown on a GGG substrate. Ce:YIG/YAG exhibited a MO figure of merit of 50°/dB at 1064 nm and 127°/dB at 1550 nm wavelength, smaller than values measured for Ce:YIG/GGG but suitable for MO devices. Ce:YIG/YAG showed a large H_c with high transmissivity in the near-IR, which is suitable for nonvolatile latching-switching devices, such as displays[7] or memory.[48] Further improvements, including the use of a buffer layer,[2] may improve the crystallinity and MO properties of Ce:YIG on YAG. This report highlights the integration of Ce:YIG on YAG, marking a significant step toward applications that combine MO materials directly with laser crystals.

See the supplementary material for the following details: the pole figure measurement of the YAG (111) substrate (Fig. S1); the refractive index and extinction coefficient spectra of the YAG (111) substrate (Fig. S2); and the smoothed FR and FE measurement results (Fig. S3).

This work was partly supported by JSPS KAKENHI Nos. 20H02593, 20K20535, and 23H01439 from the JSPS, NEDO No. 23200047-0, a TI-FRIS fellowship, and the Inamori Foundation. We also acknowledge CINTS, GIMRT, LNS, and the Fundamental Technology Center of Tohoku University. CAR acknowledges support from the NSF Award No. ECCS2028199.

AUTHOR DECLARATIONS

Conflict of Interest

The authors have no conflicts to disclose.

Author Contributions

Yuki Yoshihara: Data curation (lead); Formal analysis (equal); Software (lead). **Kazushi Ishiyama:** Supervision (supporting); Validation (supporting). **Toshiaki Watanabe:** Data curation (supporting); Investigation (supporting). **Pang Boey Lim:** Data curation (supporting); Supervision (supporting). **Mitsuteru Inoue:** Funding acquisition (equal); Validation (supporting). **Caroline A. Ross:** Validation (lead); Writing – review & editing (lead). **Taichi Goto:** Conceptualization (lead); Formal analysis (equal); Funding acquisition (equal); Methodology (equal); Project administration (lead); Software (equal); Supervision (equal); Writing – original draft (lead); Writing – review & editing (equal).

DATA AVAILABILITY

The data that support the findings of this study are available within the article and its supplementary material.

REFERENCES

[1] B. J. H. Stadler and T. Mizumoto, IEEE Photonics J. **6**(1), 0600215 (2014).
[2] L. Bi, J. Hu, P. Jiang, D. H. Kim, G. F. Dionne, L. C. Kimerling, and C. A. Ross, Nat. Photonics **5**, 758 (2011).
[3] R. Ma, S. Reniers, Y. Shoji, T. Mizumoto, K. Williams, Y. Jiao, and J. van der Tol, Optica **8**(12), 1654 (2021).
[4] K. Shimokawa, H. Dohnomae, T. Mukai, H. Yamada, H. Matsuda, and M. Daimon, J. Magn. Magn. Mater. **154**(2), 271 (1996).
[5] Z. Shirakashi, T. Goto, H. Takagi, Y. Nakamura, P. B. Lim, H. Uchida, and M. Inoue, Sci. Rep. **7**(1), 12835 (2017).
[6] K. Aoshima, K. Machida, D. Kato, T. Mishina, K. Wada, Y. F. Cai, H. Kinjo, K. Kuga, H. Kikuchi, T. Ishibashi, and N. Shimidzu, J. Disp. Technol. **11**(2), 129 (2015).
[7] K. Nakamura, H. Takagi, T. Goto, P. B. Lim, H. Horimai, H. Yoshikawa, V. M. Bove, and M. Inoue, Appl. Phys. Lett. **108**(2), 022404 (2016).
[8] H. Lee, S. Jeon, B. Friedman, and K. Lee, Sci. Rep. **7**, 43804 (2017).
[9] H. Nasuno, S. Hashi, and K. Ishiyama, IEEE Trans. Magn. **47**(10), 4011 (2011).
[10] C. Koerner, R. Dreyer, M. Wagener, N. Liebing, H. G. Bauer, and G. Woltersdorf, Science **375**(6585), 1165 (2022).
[11] O. Wojewoda, T. Hula, L. Flajšman, M. Vaňatka, J. Gloss, J. Holobrádek, M. Staňo, S. Stienen, L. Körber, K. Schultheiss, M. Schmid, H. Schultheiss, and M. Urbánek, Appl. Phys. Lett. **117**(2), 022405 (2020).
[12] H. Qin, R. B. Holländer, L. Flajšman, and S. van Dijken, Nano Lett. **22**(13), 5294 (2022).
[13] H. Qin, R. B. Holländer, L. Flajšman, F. Hermann, R. Dreyer, G. Woltersdorf, and S. van Dijken, Nat. Commun. **12**(1), 2293 (2021).
[14] R. Morimoto, T. Goto, J. Pritchard, H. Takagi, Y. Nakamura, P. B. Lim, H. Uchida, M. Mina, T. Taira, and M. Inoue, Sci. Rep. **6**, 38679 (2016).
[15] A. Kehlberger, K. Richter, M. C. Onbasli, G. Jakob, D. H. Kim, T. Goto, C. A. Ross, G. Götz, G. Reiss, T. Kuschel, and M. Kläui, Phys. Rev. Appl. **4**(1), 014008 (2015).

[16] T. Goto, R. Morimoto, J. W. Pritchard, M. Mina, H. Takagi, Y. Nakamura, P. B. Lim, T. Taira, and M. Inoue, Opt. Express **24**(16), 17635 (2016).
[17] R. Morimoto, T. Goto, T. Taira, J. Pritchard, M. Mina, H. Takagi, Y. Nakamura, P. B. Lim, H. Uchida, and M. Inoue, Sci. Rep. **7**(1), 15398 (2017).
[18] J. E. Mee, J. L. Archer, R. H. Meade, and T. N. Hamilton, Appl. Phys. Lett. **10**, 289 (1967).
[19] A. Sposito, T. C. May-Smith, G. B. G. Stenning, P. A. J. de Groot, and R. W. Eason, Opt. Mater. Express **3**(5), 624 (2013).
[20] A. Krysztofik, S. Özoğlu, R. D. McMichael, and E. Coy, Sci. Rep. **11**(1), 14011 (2021).
[21] H. Wang, C. Du, P. C. Hammel, and F. Yang, Phys. Rev. B **89**(13), 134404 (2014).
[22] R. Morimoto, T. Goto, Y. Nakamura, P. B. Lim, H. Uchida, and M. Inoue, Jpn. J. Appl. Phys. **57**(6), 061101 (2018).
[23] S.-Y. Liu, Z.-Y. Lin, Y.-R. Chang, Y.-T. Liao, P.-H. Wu, S.-Y. Huang, W.-C. Lin, and F.-Y. Lo, J. Alloys Compd. **922**, 166217 (2022).
[24] M. C. Onbasli, L. Beran, M. Zahradník, M. Kučera, R. Antoš, J. Mistrík, G. F. Dionne, M. Veis, and C. A. Ross, Sci. Rep. **6**, 23640 (2016).
[25] S. Mino, A. Tate, T. Uno, T. S. Toshihiro Shintaku, and A. S. Atsushi Shibukawa, Jpn. J. Appl. Phys. **32**(7R), 3154 (1993).
[26] A. Sposito, S. A. Gregory, P. A. J. de Groot, and R. W. Eason, J. Appl. Phys. **115**(5), 053102 (2014).
[27] A. Nakatsuka, A. Yoshiasa, and T. Yamanaka, Acta Crystallogr., Sect. B **55**(3), 266 (1999).
[28] V. F. Kitaeva, E. V. Zharikov, and I. L. Chistyi, Phys. Status Solidi A **92**(2), 475 (1985).
[29] E. Lage, L. Beran, A. U. Quindeau, L. Ohnoutek, M. Kucera, R. Antos, S. R. Sani, G. F. Dionne, M. Veis, and C. A. Ross, APL Mater. **5**(3), 036104 (2017).
[30] Y. Yoshihara, T. Sugita, P. B. Lim, Y. Tamba, H. Inoue, K. Ishiyama, M. Inoue, C. A. Ross, and T. Goto, Opt. Mater. **133**, 112967 (2022).
[31] T. Goto, Y. Eto, K. Kobayashi, Y. Haga, M. Inoue, and C. A. Ross, J. Appl. Phys. **113**(17), 17A939 (2013).
[32] S. Geller, G. P. Espinosa, and P. B. Crandall, J. Appl. Crystallogr. **2**(2), 86 (1969).
[33] P. Ghising, Z. Hossain, and R. C. Budhani, Appl. Phys. Lett. **110**(1), 012406 (2017).
[34] T. Shintaku, A. Tate, and S. Mino, Appl. Phys. Lett. **71**(12), 1640 (1997).
[35] T. Yoshimoto, T. Goto, K. Shimada, B. Iwamoto, Y. Nakamura, H. Uchida, C. A. Ross, and M. Inoue, Adv. Electron. Mater. **4**, 1800106 (2018).
[36] G. A. Jeffery, *Elements of X-Ray Diffraction*. (Cambridge University Press, Cambridge, UK, 1957).
[37] M. Gomi and T. Kanie, Jpn. J. Appl. Phys. **35**(3R), 1798 (1996).
[38] H. Kim, A. Grishin, and K. V. Rao, J. Appl. Phys. **89**(8), 4380 (2001).
[39] R. L. Comstock and J. J. Raymond, J. Appl. Phys. **38**(9), 3737 (1967).
[40] P. Hansen, J. Appl. Phys. **45**(8), 3638 (1974).
[41] M. Kubota, A. Tsukazaki, F. Kagawa, K. Shibuya, Y. Tokunaga, M. Kawasaki, and Y. Tokura, Appl. Phys. Express **5**(10), 103002 (2012).
[42] A. H. Eschenfelder, J. Appl. Phys. **49**(3), 1891 (1978).
[43] M. Kuila, A. Sagdeo, L. A. Longchar, R. J. Choudhary, S. Srinath, and V. Raghavendra Reddy, J. Appl. Phys. **131**(20), 203901 (2022).
[44] P. Hansen and K. Witter, J. Appl. Phys. **58**(1), 454 (1985).
[45] L. Soumah, N. Beaulieu, L. Qassym, C. Carrétéro, E. Jacquet, R. Lebourgeois, J. Ben Youssef, P. Bortolotti, V. Cros, and A. Anane, Nat. Commun. **9**(1), 3355 (2018).
[46] M. Gomi, H. Furuyama, and M. Abe, J. Appl. Phys. **70**(11), 7065 (1991).
[47] N. Fairley, V. Fernandez, M. Richard-Plouet, C. Guillot-Deudon, J. Walton, E. Smith, D. Flahaut, M. Greiner, M. Biesinger, S. Tougaard, D. Morgan, and J. Baltrusaitis, Appl. Surf. Sci. Adv. **5**, 100112 (2021).
[48] Y. Nakamura, H. Takagi, P. B. Lim, and M. Inoue, Opt. Express **22**(13), 16439 (2014).